AlgaeNet: A Deep-Learning Framework to Detect Floating Green Algae From Optical and SAR Imagery

Le Gao, *Member, IEEE*, Xiaofeng Li, *Fellow, IEEE*, Fanzhou Kong, Rencheng Yu, Yuan Guo, *Student Member, IEEE*, and Yibin Ren, *Member, IEEE*

***Abstract*—This article developed a scalable deep-learning model, the AlgaeNet model, for floating Ulva prolifera (*U. prolifera*) detection in moderate resolution imaging spectroradiometer (MODIS) and synthetic aperture radar (SAR) images. We labeled 1055/4071 pairs of samples, among which 70%/30% were used for training/validation. As a result, the model reached an accuracy of 97.03%/99.83% and a mean intersection over union of 48.57%/88.43% for the MODIS/SAR images. The model was designed based on the classic U-Net model with two tailored modifications. First, the physics information input was a multichannel multisource remote sensing data. Second, a new loss function was developed to resolve the class-unbalanced samples (algae and seawater) and improve model performance. In addition, this model is expandable to process images from optical sensors (e.g., MODIS/GOCI/Landsat) and SAR (e.g., Sentinel-1/GF-3/Radarsat-1 or 2), reducing the potential biases due to the selection of extraction thresholds during the traditional threshold-based segmentation. We process satellite images containing *U. prolifera* in the Yellow Sea and draw two conclusions. First, adding the 10-m high-resolution SAR imagery shows a 63.66% increase in algae detection based on the 250-m resolution MODIS image alone. Second, we define a floating and submerged ratio number (FS ratio) based on the floating and submerged parts of *U. prolifera* detected by SAR and MODIS. A research vessel measurement confirms the FS ratio to be a good indicator for representing different life phases of *U. prolifera*.**

***Index Terms*—Deep learning (DL), green algae detection, satellite remote sensing.**

Manuscript received January 18, 2022; revised February 21, 2022; accepted March 22, 2022. Date of publication March 25, 2022; date of current version April 19, 2022. This work was supported in part by the National Natural Science Foundation of China under Grant U2006211 and Grant 42090044, in part by the Major Scientific and Technological Innovation Projects in Shandong Province under Grant 2019JZZY010102, in part by the Strategic Priority Research Program of the Chinese Academy of Sciences (CAS) under Grant XDA19060101 and Grant XDB42000000, in part by the Key Project of the Center for Ocean Mega-Science under Grant COMS2019R02, in part by the CAS Program under Grant Y9KY04101L, and in part by the Zhejiang Provincial Natural Science Foundation of China under Grant LR21D060002. *(Corresponding author: Xiaofeng Li.)*

Le Gao, Xiaofeng Li, Yuan Guo, and Yibin Ren are with the Key Laboratory of Ocean Circulation and Waves, Institute of Oceanology, CAS and Center for Ocean Mega-Science, CAS, Qingdao 266071, China (e-mail: gaole@qdio.ac.cn; lixf@qdio.ac.cn; guoyuan201@mails.ucas.ac.cn; yibinren@qdio.ac.cn).

Fanzhou Kong and Rencheng Yu are with the Key Laboratory of Marine Ecology and Environmental Sciences, Institute of Oceanology, CAS and Center for Ocean Mega-Science, CAS, Qingdao 266071, China (e-mail: fzkong@qdio.ac.cn; rcyu@qdio.ac.cn).

Digital Object Identifier 10.1109/JSTARS.2022.3162387

I. Introduction

HARMFUL algal blooms, including red/brown tides caused by microalgae and green/golden tides caused by macroalgae, are disastrous ecological events in coastal oceans. For example, in the waters along the coast of China in the Yellow Sea, macroalgae blooms formed by massive floating green alga Ulva prolifera (*U. prolifera*) have been recorded in the spring–summer season since 2007 [1]–[3]. The rapid biomass increase severely impacts the environment, coastal ecosystems, public health, ship traffic, the local tourism industry, and even the 2008 Olympic regatta games [4]–[11].

Satellite remote sensing is the primary *U. prolifera* detection approach due to the advantages of frequent data acquisition and broad coverage area [3], [12]. Existing studies mostly use moderate resolution imaging spectroradiometer (MODIS) images acquiring the visible and infrared bands at a spatial resolution of 250–1000 m. The floating *U. prolifera* modulates the ocean color properties and shows the prominent algae features in MODIS images that lead to significant progress in evaluation and prediction of the blooming mechanism of the algae [3], [13]–[15]. However, previous articles have pointed out that the algae biomass extracted from coarse-resolution images has a certain degree of error [3], [16], making it difficult to quantify the algae patches missed in an optical image. Evaluating and reducing this extraction error through image resolution have become a bottleneck problem for algae detection in optical remote sensing.

Synthetic aperture radar (SAR) is an active remote sensing radar that provides sea surface roughness images at tens of meters in spatial resolution, an order of a magnitude higher than MODIS, under all weather conditions, day and night. SAR does not have in-water penetration capability and receives the surface normalized radar cross-section (NRCS) backscattering signal related to the Bragg wave spectrum modulated by ocean surface wind, waves, and currents. The floating algae on the sea surface behave like a hard object. The NRCS is no longer a backscattering signal but a reflected signal due to the double- or triple-bounce effect. As a result, the algae patch area's reflected signal is much stronger than that backscattered one from the surrounding water, which appears as brighter regions in SAR images. Currently, the European Space Agency (ESA) Sentinel-1 and Chinese GF-3 SAR data have become accessible and open, making SAR another option for detecting algae and other marine targets like ships and oil spills [17]–[19].

This work is licensed under a Creative Commons Attribution 4.0 License. For more information, see https://creativecommons.org/licenses/by/4.0/

The disadvantage of SAR mainly lies in the limited temporal coverage. Nevertheless, SAR and MODIS can accommodate each other for algae detection. SAR has a higher spatial resolution than MODIS and avoids the influence of mixed pixels containing both algae and seawater in the MODIS image.

There are many different methods to detect algae. For optical-sensor images, biological index methods, e.g., NDVI (normalized difference vegetation index) and FAI (floating algae index), are commonly used [12], [20]. For SAR-sensor images, we usually use grey or backscatter coefficient differences to identify the target [17], [19]. These traditional methods have advantages, but they cannot effectively fuse the two data sources. To perform data fusion based on the algae's characteristics captured by the two sensors, deep learning (DL) offers one possibility [21]. In recent years, DL has been extensively applied in the fields of ocean oil spills [22], internal waves [23], ocean ships [24], sea ice [25], and time-space prediction [26], [27].

U. prolifera algae is bright or dark green due to a large amount of chlorophyll in the cells. Some parts of the algae body are exposed above the sea surface during its blooms, while others are submerged. An optical sensor can collect spectral information at a certain sea depth to effectively capture the floating and underwater parts of the algae [16], [28]. By contrast, the SAR sensor captures only the floating part on the sea surface. Thus, the floating and submerged algae ratio (FS ratio = SAR/MODIS) can be estimated. The FS ratio may become an indicator to differentiate the life phases of *U.prolifera* [29], [30].

The objectives of this article include 1) developing a DL network to better mine *U. prolifera* information from optical and SAR images, 2) evaluating the degree of algae underestimation in coarse-resolution optical images, and 3) estimating their life stages using the algae FS ratio. The article is organized as follows. Section II introduces related datasets, including optical MODIS data, microwave SAR data, and the relevant ship survey data. Section III introduces the proposed DL network model, including training labels, physical model optimization, and model performance verification. Section IV introduces our findings after using the proposed DL model for multisource optical and SAR data fusion. Discussions and conclusions are in Sections V and VI.

II. Data Used

A. Satellite Observations

MODIS is a key sensor aboard the National Aeronautics and Space Administration Terra and Aqua satellites with a sweeping 2330-km wide viewing swath. We collected 112 MODIS images containing algae patches under clear sky conditions in the Yellow Sea from 2008 to 2021, shown in Fig. 2(a)–(c). These MODIS images are geometrically and radiometrically corrected 250-m spatial resolution true-color imagery (Bands: 1/4/3). Of course, the NIR band is useable. However, we use true-color images as the data source for the following reasons:

1) True-color image is relatively easy for manual labeling. Using the labeling results of true-color images as the ground truth to train the model is typical for neural network classification. Especially, true-color image product is usually standard product from MODIS-like sensors. Therefore, our model can be readily applied to similar images without modification.
2) The proposed model framework can also be extended to include data from different satellites and sensors (e.g., NIR and IR) without significant modification.
3) Our model can also find small algae patches in satellite images. Still, small algae patches will have more significant uncertainty when calculating the FS ratio, so we pay more attention to the big algae patches. Inevitably, some tiny algae pixels may be missed in coarse resolution optical images. Therefore, the algae-containing pixels were extracted, and the fractional areal coverages were quantified using a simple unmixing method of the DL model's output possibility.

The SAR images are from the ESA's Sentinel-1 (92 images) and Chinese GF-3 (31 images) satellites, shown in Fig. 2(d). We used Sentinel-1 Level-1 ground range detected dual-polarization (VV and VH) interferometric wide images with 10-m spatial resolution and 250-km swath and the Chinese GF-3 SAR fine stripe mode II dual-polarization (HH and HV) image with 10-m resolution and 100-km swath. All SAR images were acquired between 2015 and 2019. We applied speckle filter and geometric/radiometric/orthometric corrections to the SAR images. The Sentinel Application Platform 7.0 software is used. In addition, we also performed a standard deviation stretch with the gamma value of the SAR image to give the image an acceptable dynamic range.

B. Ship Survey Data

The *U. prolifera* bloom at various life stages may show considerable differences in different morphological characteristics [30], [31]. We tried to use the FS ratio as an indicator to distinguish the life phases of *U. prolifera* blooms. To verify the FS ratio's feasibility, data acquired during a comprehensive ship survey along the 35°N cross-transect in the Yellow Sea on June 9, 10, 20, and 21, 2017, shown in Fig. 1(a) and (d), were used. The research vessel, "Science-III," traveled at 2.5 nautical miles/h and trawled floating algae at various stations along the survey transect for 5 min. Once the floating alga picked up by the trawler were transferred to the deck and wiped dry, they weighed immediately on beam scales of different specifications. Finally, the total biomass of the floating algae along the 35°N section is obtained. The algae biomass at various stations shows different spatial distribution characteristics. When algae bloom on a large scale, the algae bodies gather together, resulting in high algae density per unit area. The survey ship is sailing to collect the algae slicks. When the ship travels to an area with a high (low) density, the collected algae biomass will be large (small), so the biomass in each station also shows the distribution characteristics of algae [Fig. 1(b)–(d)]. Meanwhile, the density (biomass) of different algae is also related to their life state [14]. The life process of *U. prolifera* in the Yellow sea is well known in the research community, originating in Jiangsu coast, drifting northward, and disappearing along the coast of Shandong. This article

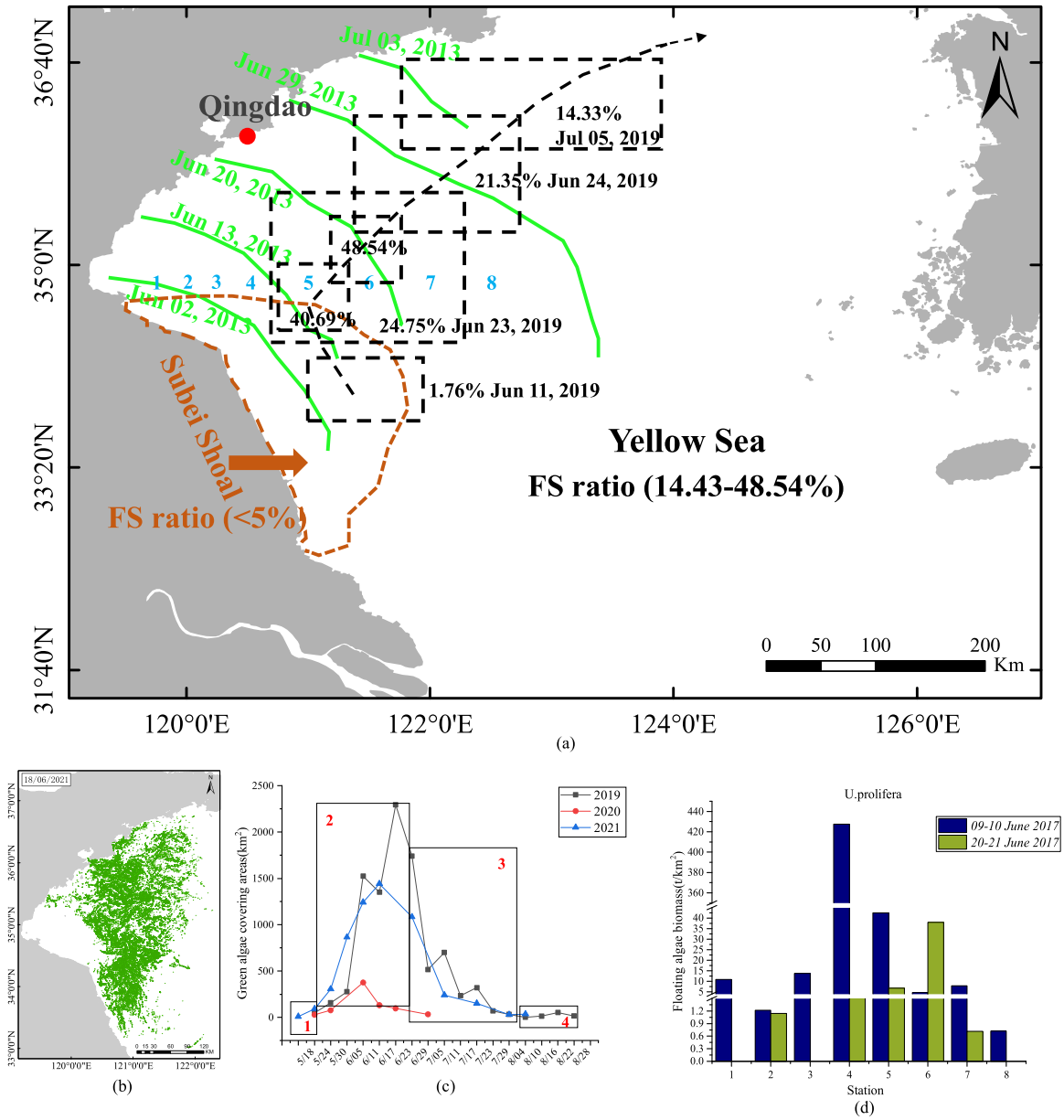


Fig. 1. Yellow Sea *U. prolifera* macroalgal detection and life status indicator changes of macroalgal bloom. (a) Time series of detected macroalgae patches coverage based on the AlgaeNet model. The green solid lines are the northern boundary of the algae distribution range along the drifting direction throughout the algae bloom cycle in 2013. The brown dash line is the Subei Shoal's location, and the black dash boxes are the estimated FS ratio. (b)–(c) Largest algae coverage in 2021 and coverage changes in the initiation (1), rapid development (2), maintenance (3), and diminishing (4) phases from 2019 to 2021. (d) Algae biomass at various stations [the eight numbers in Fig. 1(a)] by ship survey in the maintenance and diminishing phase of the *U. prolifera* bloom.

found that FS ratios in different areas are different in the entire drift path. As a result, we used the FS as a life-stage indicator.

III. DL-Based Algae Detection Model

A. Training Labels

In MODIS images, the *U. prolifera* algae pixels show more prominent green slick/patch features compared to the surrounding seawater pixels [Fig. 2(a)]. Therefore, we can label sample image slices containing different algae shapes (banded, lumpy, and dotted) using the Lableme software (Fig. 2(b), [32]) for DL algorithm development. To expand the sample size, we followed a common practice in the artificial intelligence field and rotated the labels 90°, 180°, and 270° to create new labels. Among the 1055 pairs of MODIS image slices and corresponding labels, 972/83 pairs were used as training/testing sets. The training set was divided into 70% for training and 30% for validation in the training process. We found that the composite false-color image (with infrared, red, and green bands) and the true-color image (with red, green, and blue bands) have almost the same algae–seawater contrast characteristics under cloud-free and high image quality conditions. Therefore, it is sufficient to annotate the training/testing dataset using true-color images. In particular, some "suspected algae pixels" with low

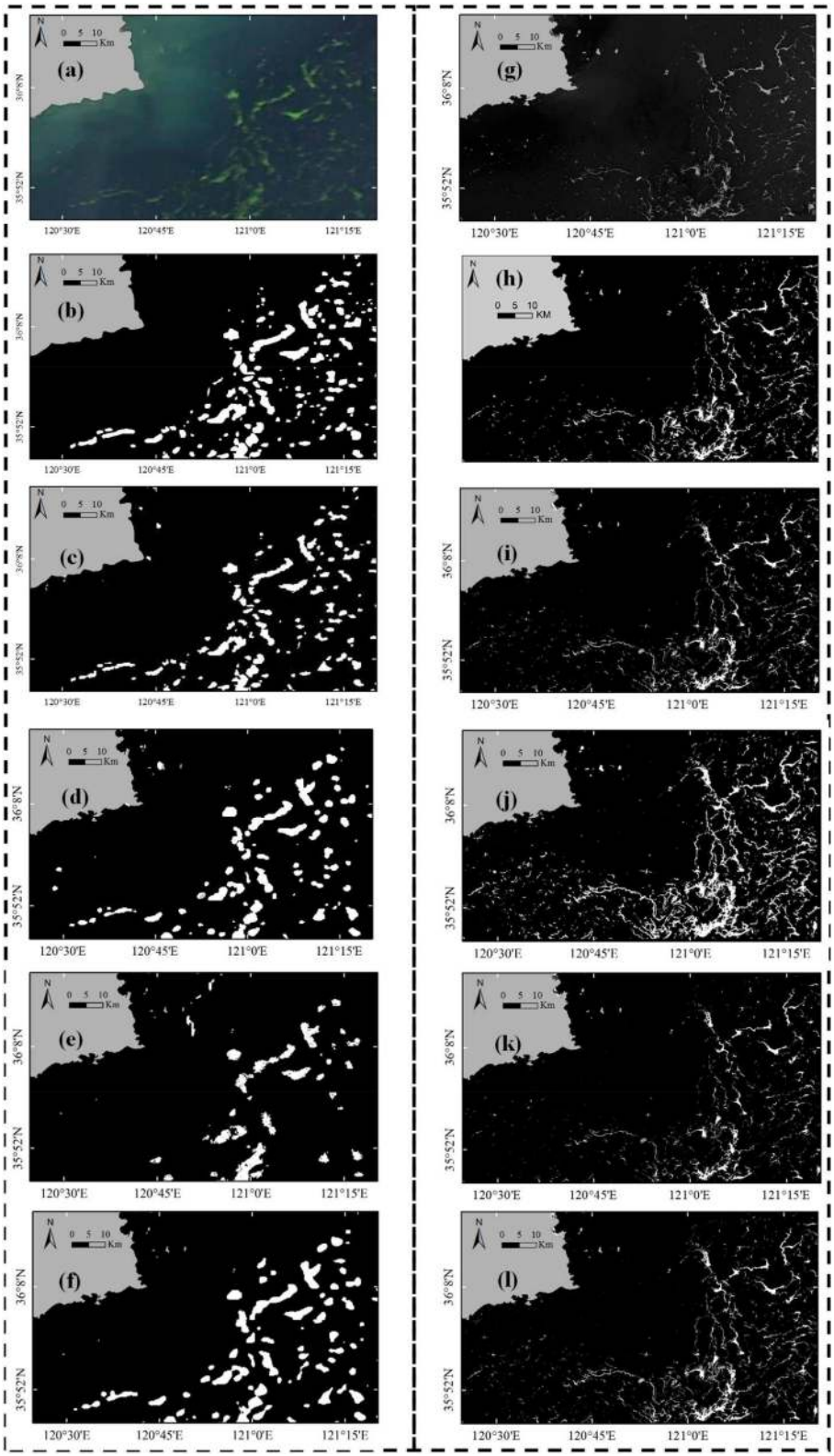


Fig. 2. *U. prolifera* macroalgae detection in MODIS and SAR images at the pixel level in a bloom period: (a) Randomly selected MODIS true-color image slice in the Yellow Sea on June 23, 2019; (b) Manual ground truth based on the MODIS image clip; (c)–(f) Corresponding predicted value of the AlgaeNet, classic UNet, RF, and VGG16 models; (g) Corresponding SAR slice on June 23, 2019; (h) Manually marked ground truth based on the SAR image clip; (i)–(l) Predicted value based on the AlgaeNet, classic UNet, RF, and VGG16 models for SAR imagery, respectively. In subfigures (b)–(l), The white dots are algae pixels, and the black color is the background ocean.

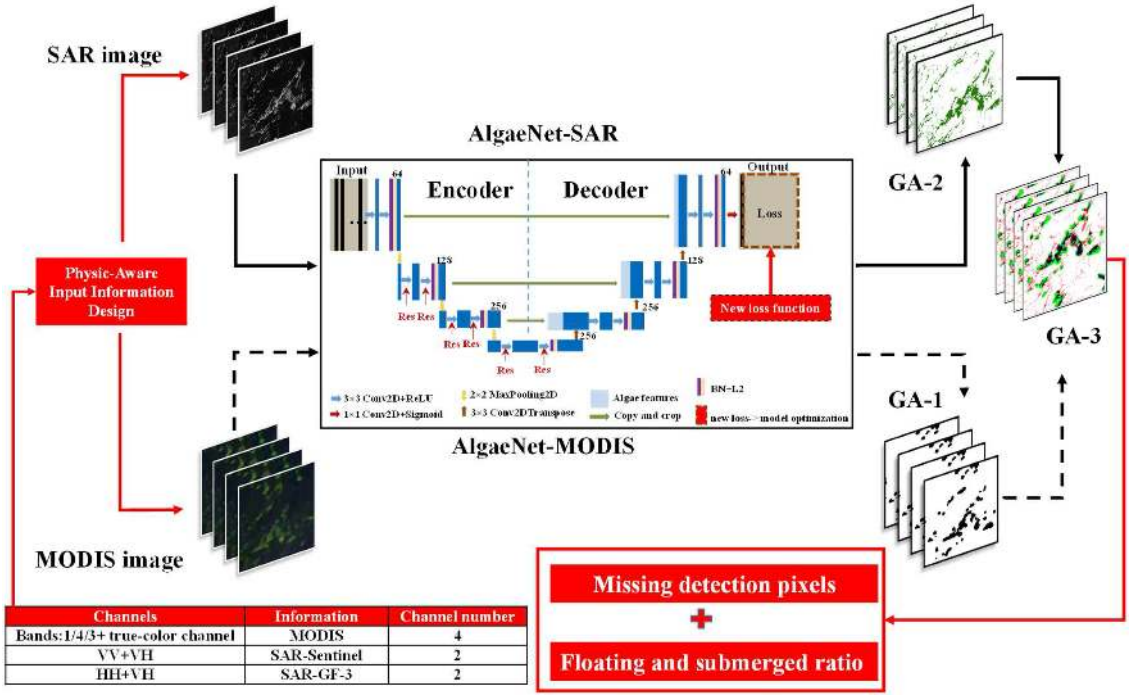


Fig. 3. Flowchart of the proposed AlgaeNet model to assess missing macroalgae and distinguish life stages. The specially tailored modifications to U-Net are highlighted. GA-1 represents the algae pixels identified in the optical image, GA-2 represents the algae pixels identified in the SAR image, and GA-3 represents the fusion result of GA-1 and GA-2.

algae–seawater contrast were excluded when labeling. Although the contrast of algae–seawater is much more prominent in the infrared band than in the green band, the composite true-color image is more robust than a pure one-band channel image.

In SAR images, the algae patches show bright white spots and slicks shown in Fig. 2(g). We marked the algae's image slices and corresponding labels [Fig. 2(h)]. A total of 4071 pairs of image slices and their related labels were obtained, 2981 pairs were used as training sets (70% for training and 30% for validation), and 1090 pairs were used as testing sets.

We have considered the possible overlap between the labeling training/validation/testing sets. Therefore, MODIS data from 2008–2018/2019-2020/2021 are used as the training/validation/testing set. Similarly, for SAR, the 2015–2017/2018/2019 data for the training/validation/testing data. Thus, in the train/validation set, there is no overlap and spatial adjacency, and it does not affect the training and validation of the DL model.

B. DL-Based Algae Detection Network (AlgaeNet)

We propose a comprehensive multisource data processing and fusion method based on the DL technique to detect the algae areas better. DL has unique advantages in the image classification and segmentation field. Robust DL models include Random forest (RF), U-Net, Densenet, GoogleNet, ResNet, VGG, and others [21], [33]–[36]. The U-Net framework can integrate features of different levels and avoid the large sample training requirements. Fig. 3 shows our customized model's system diagram based on the U-Net framework [21], [33]. Optical and SAR data are input separately, and the model can perform data fusion based on the difference between the two sensors' detection results. All pixels of the entire area are divided into four categories: 1) seawater pixels; 2) algae pixels that can only be identified in the optical image; and 3) algae pixels that can only be identified in SAR images. The FS ratio can be calculated by the two pixels of (2) and (3); (4) is the small algae patches pixels that can be recognized by only SAR but not optical image, and it corresponds to the missing algae detection in the optical image. Our model has a freely expandable design to process data from other optical sensors like GOCI and Landsat, and SAR sensors like Envisat and Radarsat-1/2. To make a distinction, the model trained using MODIS imagery is called AlgaeNet-MODIS and that for SAR is AlgaeNet-SAR. We refer to the overall DL architecture as AlgaeNet.

In the training samples, algae patch and seawater are two classification types. Algae detection is essentially a binary classification problem—specifically, an unbalanced class problem. The number of algae pixels is small compared with seawater pixels. This fact may cause the DL model to learn seawater features instead of algae features. Therefore, based on U-Net, we made two special modifications to improve our model performance as follows:

1) Our model includes a physics information input design. DL simulates the human visual system and extracts features layer by layer from color pictures, generally using true-color images as direct input, typical in the field of computer vision [34], [35]. However, for algae detection, the combination of several MODIS bands is effective, e.g., the FAI/NDVI biological indices methods [12], [20].

TABLE I
ACCURACY ASSESSMENT OF ALGAENET MODEL

Input Data	AI-Model	Output (%)				
		Accuracy	Precision	Recall	F1 score	Mean IoU
MODIS	Classic U-Net	96.37	62.96	53.84	58.04	37.89
	Random Forest	95.29	55.78	14.12	22.53	12.69
	VGG16	96.76	66.57	61.25	63.79	47.82
	AlgaeNet	97.03	75.36	57.73	65.38	48.57
Sentinel-1/GF-3 SAR	Classic U-Net	99.81	94.65	91.65	93.13	87.14
	Random Forest	99.39	72.95	87.96	79.75	66.60
	VGG16	99.82	93.94	88.44	91.11	87.83
	AlgaeNet	99.83	95.46	92.32	93.86	88.43

Therefore, we combine channel and true-color data to achieve better algae detection. For SAR, we combine the two polarization channels of VV (HH) and VH (HV) as input to perform the dual-polarization fusion that leads to improved algae detection accuracy [36].

2) We implemented a new loss function design. The new loss function addresses the unbalanced sample problem. Because algae detection is a binary classification problem, binary-cross entropy (BCE) is usually used as the loss function. However, compared with the ocean background, the algae detection is more of an unbalanced classification problem because algae patches may occupy a small proportion of the overall image. Therefore, using only the "Accuracy" index cannot wholly evaluate the model [36]. To get a better model, we defined a new loss function for the AlgaeNet model, shown as formulas 1 and 2, to solve unbalanced sample categories:

$$F1 = (2 * P * R)/(P + R) \tag{1}$$

$$\text{loss} = \alpha \text{BCE} + (1 - \alpha)(1 - F1) \tag{2}$$

where P denotes "precision," R denotes "recall," and $F1$ denotes the macro $F1$ score. When we calculate the $F1$ score, we use the probabilities instead of integers 0/1 and this transformation makes the macro $F1$ score function continuous and differentiable[1] BCE denotes binary-cross entropy, and αdenotes the balance factor between $F1$ and BCE. We tried the influence of different balance factors on the neural network in the experiment, and the neural network was optimal when the balance factor was defined as 0.2.

C. AlgaeNet Performance

The performance evaluation of the AlgaeNet model can be divided into two parts, namely, the assessments of the detection performance of AlgaeNet-MODIS and AlgaeNet-SAR.

[1][Online]. Available: https://www.kaggle.com/rejpalcz/best-loss-function-for-f1-score-metric

For evaluating the AlgaeNet-MODIS model, we first used 83 MODIS testing labels to quantitatively compare the AlgaeNet-MODIS model's accuracy with that of the classic U-Net model. Table I shows that the performance of the AlgaeNet-MODIS model is better than the original U-Net model; the AlgaeNet-MODIS (U-Net) model reached 97.03 (96.37)%, 75.36 (62.96)%, 57.73 (53.84)%, 65.38 (58.04)%, and 48.57 (37.89)% in the five commonly used indicators of Accuracy, Precision, Recall, $F1$_Score, and mean intersection over union. Accuracy refers to the proportion of correctly predicted algae pixels among all predicted pixels. Precision refers to the proportion of pixels that are true algae and predicted as algae to all predicted algae pixels. A higher precision value means the model extracts fewer false alarms. Recall refers to the proportion of true algae pixels and predicts as algae to all true algae pixels. A higher recall value means the model misses fewer algae pixels. Finally, IoU means the proportion of true algae and predicted algae to the union of true algae and predicted algae pixels. When the predicted algae pixels coincide entirely with the true algae pixels, the IoU has the maximum value of 1. The evaluation indicators are shown in formula (3). Fig. 2(a)–(f) also shows the algae detection performance in the *U. prolifera* blooming period. By comparing the subimages (b) and (c) of the ground truth and the predicted value of the DL-based models, the prediction map is very close to the ground truth, which visually confirms the effectiveness of the proposed method. "Ground truth" refers to the labels manually annotated based on the analyst's visual interpretation using the Lableme software [25], [32]. This procedure is a common practice in creating labels. We also compared the AlgaeNet-MODIS model with the traditional biological index method. After the DL-based model is trained, the threshold of the proposed AlgaeNet model is determined and cannot be changed, e.g., the pixels with output probabilities > 0.5 are determined as algae-containing pixels. Subsequently, this threshold was applied to other remote sensing images to detect algae. It cannot be changed. The decision is based on the optimized model weights learned from the training processes. Still, the index-based threshold can be changed. For example,

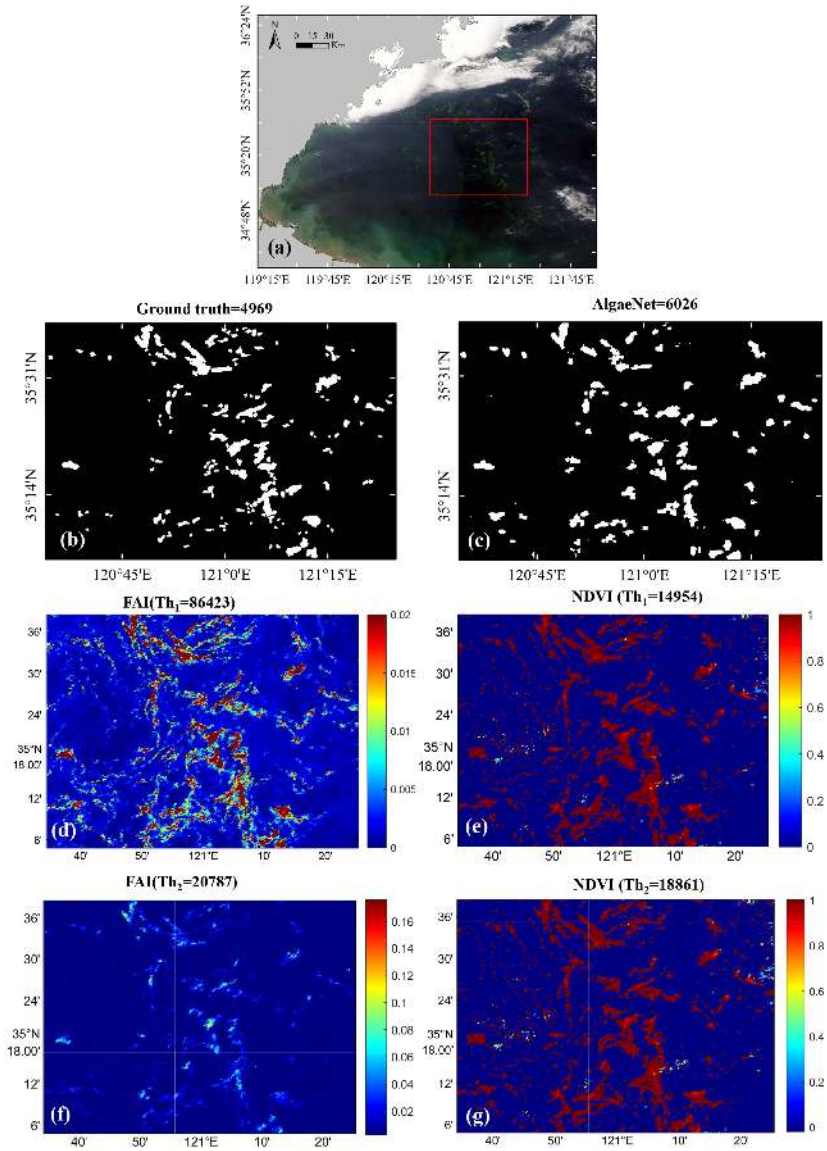


Fig. 4. Comparison result of the AlgaeNet model and traditional biological index methods: (a) MODIS imagery; (b) manually marked ground truth based on the MODIS image clip (red box in figure a); (c) detected algae pixels based on the AlgaeNet model on July 09, 2021; (d) and (f) corresponding algae pixels detected by the FAI method (threshold: $0 < \text{FAI}\ (\text{Th}_1) < 0.02$; $0.0025 < \text{FAI}\ (\text{Th}_2) < 0.176$); (e) and (g) corresponding algae pixels detected by the NDVI method (threshold: $\text{NDVI}\ (\text{Th}_1) > 0$; $\text{NDVI}\ (\text{Th}_2) > -0.02$).

FAI has two thresholds (0, 0.02) or (0.0025, 0.176), which can be selected according to the different scenes: the second threshold is usually used to unmix the algae coverage, only the first threshold is used to identify the algae pixels. The DL-based model would reduce the potential biases due to selecting extraction thresholds of FAI or NDVI. We used the FAI/NDVI method to detect algae pixels and coverage with the recommended threshold [3], [37], [38]. We investigated the MODIS data available in July 2021. Fig. 4(a) shows the MODIS true-color image in the Yellow Sea on July 9, 2021. The floating algae appear a light green color. Our method and two index methods (FAI and NDVI) confirmed that these colored patches are floating green algae [Fig. 4(b)–(d)]. By our DL model, 6026 algae pixels were identified. The number of algae pixels identified by the FAI index method was 86 423 and 20 787 when (0, 0.02) and (0.0025, 0.175) were set as thresholds, and the number of algae pixels identified by the NDVI index method was 14 954 and 18 861 when >0 and >-0.2 were set as thresholds. The FAI and NDVI methods have considerable uncertainty because of the selection of varying thresholds; even the algal identification results may differ by order of magnitude [1]–[3], [37]. The AlgaeNet model and index-based methods in this article detect different algae pixel numbers and corresponding coverage. The main reasons are as follows:

1) Different references give different algae threshold ranges. For example, with different threshold ranges, the algae coverage calculated by Xu *et al.* is about eight times of Qi's [2], [37], so some algae pixels detected by the FAI/NDVI index may be false or fake algae pixels. We should pay special attention to the fact that the false or fake pixels mentioned here are only relative to the

TABLE II
COMPARISON OF ALGAENET/FAI/NDVI

Input Data	AI-Model	Output (%)				
		Accuracy	Precision	Recall	F1 score	Mean IoU
MODIS	AlgaeNet	96.18	60.04	72.81	65.81	49.04
	FAI (Th_2)	81.87	20.43	89.27	33.25	19.94
	NDVI (Th_1)	87.93	27.79	86.86	42.11	26.67

manually marked ground truth. They do not represent the reality because some studies may more agree with the index-based result as a ground truth. Therefore, the prerequisite for our comparison is to admit that the manual labeling result is credible. This approach is also generally accepted for the DL-based model and relatively simple basis for comparison. After all, there is no other more suitable third party as the ground truth. We also conduct the metric comparison between AlageNet and indexes methods on the algae-bloom day. The strength of DL-based approaches vs. the index-based methods is that DL methods can get high Precision and Recall simultaneously. In contrast, index-based methods have to sacrifice one for the other (Table II).

2) The difference in the number of algae pixels detected by different methods is also related to different physics information input. The AlgaeNet neural network model uses the RED/GREEN/BLUE (1/4/3) bands. In contrast, FAI uses the other three channels in RED/NIR/SWIR (1/2/6) bands, and NDVI uses the two channels in the RED/NIR (1/2) bands. However, the coverage and pattern of algae patches obtained by the three methods are almost identical in our selected images.
3) Many small algae pixels were detected by FAI and NDVI methods but not by the AlgaeNet model. The reason was when we made the label dataset, we did not label some "suspected" pixels with great uncertainty due to low algae–water contrast, and they are directly discarded or treated as seawater pixels. Therefore, AlgaeNet also ignores "suspected or fake algae" features. Our goal is that the algae-containing pixels detected by AlgaeNet are "real" algae and not suspected algae pixels to reduce uncertainty

$$\begin{cases} \text{Accuracy} = \frac{\text{TP}+\text{TN}}{\text{TP}+\text{FP}+\text{TN}+\text{FN}} \\ \text{Precision} = \frac{\text{TP}}{\text{TP}+\text{FP}} \\ \text{Recall} = \frac{\text{TP}}{\text{TP}+\text{FN}} \\ \text{F1score} = \frac{2*\text{Precision}*\text{Recall}}{\text{Precision}+\text{Recall}} = \frac{2\text{TP}}{2\text{TP}+\text{FN}+\text{FP}} \\ \text{IoU} = \frac{\text{TP}}{\text{TP}+\text{FN}+\text{FP}} \end{cases} \tag{3}$$

where TP, FP, FN, and TN are the numbers of true positive samples, false positive samples, false negative samples, and true negative samples, respectively. Please note: As a metric, the regular F1 score is used, while when constructing the loss function, the macro $F1$ score is used to make it continuous and differentiable.

For the evaluation of AlgaeNet-SAR, based on the 1090 pairs of testing labels, the model reached 99.83%, 95.46%, 92.32%, 93.86%, and 88.43% in the five indicators of Accuracy, Precision, Recall, $F1$ score, and mean IoU, which is significantly better than AlgaeNet-MODIS. In particular, in terms of the comprehensive precision index of mean IoU, the AlgaeNet-SAR model's mean IoU (88.43%) is twice that of AlgaeNet-MODIS (48.57%) because the resolution of SAR is higher, and the "algae–seawater" contrast signal in the image is more substantial. However, the 48.57% accuracy already means that AlgaeNet-MODIS is superior for algae detection [39]. There are two reasons as follows:

1) The algae–seawater contrast in the visible image is weaker than SAR images due to the different imaging mechanisms (passive vs. active). Especially in the edge area of algae distribution and coverage, the overall detection effect is weaker than that of the SAR image due to coarse resolution.
2) The lower the resolution, the less the optical image grid number per unit area and the greater the random error in the grid.

Under the condition that the data sources are all MODIS, through the horizontal comparison of DL models (classical U-Net vs. AlgaeNet), we found that the improvement of IoU is still pronounced ($37.89 \geq 48.57\%$). Moreover, when the SAR image is used as the data source, the AlgaeNet's IoU reaches a very high value (88.43%), indicating the model's superior performance. Fig. 2(g)–(l) also gives a visual presentation of the algae detection performance. By comparing subimages (h) and (i), the prediction map is very close to the ground truth, which also confirms the effectiveness of the proposed method. We compared the model's further quantitative evaluation with the recent neural networks: RF and CNN-VGG16 models. Table I and Fig. 2(j)–(l) show that our model has significantly higher performance than the RF model. When we applied the multichannel combination input and the newly constructed loss function to the CNN-VGG16 model, we also achieved a high accuracy similar to AlgaeNet, indicating the excellent portability of our particular improvement strategy in various convolutional networks.

IV. RESULTS

A. Small-Patch Algae Not Detected in the MODIS Images and FS Ratio of the Algae

We used the AlgaeNet model to process the collected 112 MODIS images and 123 SAR images and acquired 12 pairs of spatiotemporal matching MODIS and SAR images/slicks (Table III). Fig. 5(a) and (b) shows two MODIS and SAR images

TABLE III
SMALL-PATCH ALGAE NOT DETECTED IN THE MODIS IMAGES AND FS RATIO OF THE ALGAE

NO.	Area	Date	Location	Missing detection rate (%)	FS ratio (%)
1	Yellow Sea	2015-07-25	Lat: 35.04°-36.43°N Lon: 119.30°-120.77°E	51.06	28.86
2	Yellow Sea	2017-06-02	Lat: 34.22°-37.02°N Lon: 119.18°-123.67°E	60.42	20.87
3	Yellow Sea	2019-06-23	Lat: 34.41°-35.71°N Lon: 119.15°-122.51°E	76.83	24.75
	Yellow Sea（1）	2019-06-23	Lat: 34.41°-35.71°N Lon: 119.15°-122.51°E	49.63	48.54
	Yellow Sea（2）	2019-06-23	Lat: 34.41°-35.71° N Lon: 119.15°-122.51°E	61.40	40.69
4	Yellow Sea	2019-06-24	Lat: 35.39-37.06°N Lon: 120.31°-122.83°E	48.74	21.35
5	Yellow Sea（1）	2019-07-05	Lat: 34.72°-37.52°N Lon: 119.24°-123.73°E	80.83	19.19
	Yellow Sea（2）	2019-07-05	Lat: 34.72°-37.52°N Lon: 119.24°-123.73°E	82.09	14.43
	Yellow Sea（3）	2019-07-05	Lat: 34.72°-37.52°N Lon: 119.24°-123.73°E	69.45	22.02
6	Yellow Sea	2019-07-11	Lat: 35.61°-37.56°N Lon: 120.13°-122.92°E	56.13	29.02
7	Yellow Sea	Mean*	/	63.66	26.97
		Range*	/	48.74-82.09	14.43-48.54
8	Subei Shoal	2018-06-23	Lat: 33.68°-34.79°N Lon: 120.11°-121.64°E	/	4.76
9	Subei Shoal	2019-06-11	Lat: 33.84°-34.47°N Lon: 120.12°-121.10°E	/	1.76

*The "Mean" refers to the average value of the missing detection rate and FS ratio calculated for the matching MODIS/SAR image pairs at different times in the Yellow Sea. The "Range" refers to their variation range of the missing detection rate and FS ratios.

during the large-scale *U. prolifera* bloom in the Yellow Sea. Fig. 5(c) and (d) shows that the algae patch from both MODIS and SAR sensors have a highly consistent spatial distribution pattern (see details in subareas 1 and 2) with two different interesting details. First, some small floating algae patches without a large aggregation degree can only be detected in the SAR imagery but not in the MODIS imagery. Second, for the big algae patches/slicks with a high aggregation degree, the margin of the algae patches observed by the MODIS sensor is broader than that observed by the SAR sensor, shown as the overlapping area inside the selected polygon in Fig. 5(d).

SAR sensors can identify more detailed algae patches due to their very high resolution. Since MODIS is the primary sensor for algae monitoring, we need to estimate how much tiny algae was not detected by MODIS alone. According to the difference between the two sensors' detection results, the AlgaeNet model performs data fusion and divides all image pixels into four categories: seawater pixels (white), algae pixels simultaneously detected by both MODIS and SAR (black), by SAR but not by MODIS (red), and by MODIS (green), shown in Fig. 5(d). When the number of algae identified by SAR is used as the actual total number of algae in the sea area (marked as N) and the number of algae identified by MODIS (marked as M), the missing detection rate is (N-M)/N. The broader margin of algae patches observed by MODIS compared to SAR is due to the two sensors' different algae detection mechanisms (see the discussion part, and we eliminated the impact of coarse resolution and overpass time difference). SAR can only detect the floating algae patches on the surface, whereas the optical MODIS sensor can detect the floating and submerged parts [16], [28]. Therefore, the FS ratio can also be estimated, i.e., M/N. Table III shows the statistical analysis of the 10 pairs of matching MODIS and SAR images/slices in the Yellow Sea. One can see that adding high-resolution SAR image information leads to an average increase of 63.66% (48.74%–82.09%) in algae detection compared to that based on the MODIS image

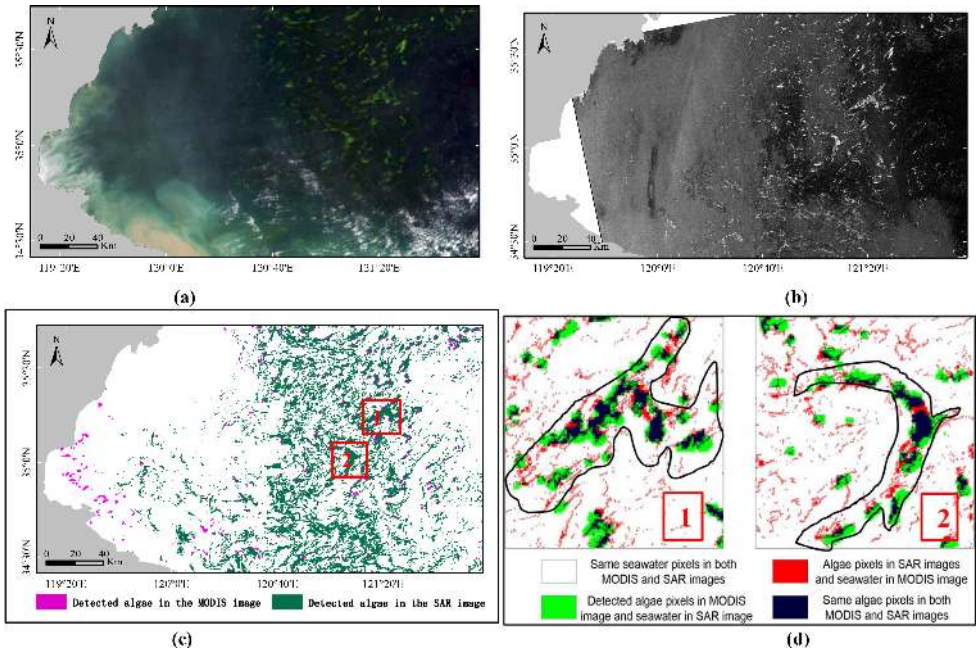


Fig. 5. Assessment of missing Yellow Sea macroalgae and FS ratio estimation: (a) and (b) MODIS and Sentinel-1 SAR images on June 23, 2019; (c) detected algae pixels between MODIS and SAR images, performed algae patch registration due to small drift and deformation using the simple rubber sheeting method; (d) four types of pixels based on the difference between optical- and SAR-sensor-detected algae to estimate the missing algae inspection rate and FS ratio. The red dots represent the missing algae pixels in the MODIS image. The figure also corresponds to the enlarged view of two randomly selected subareas (1) and (2).

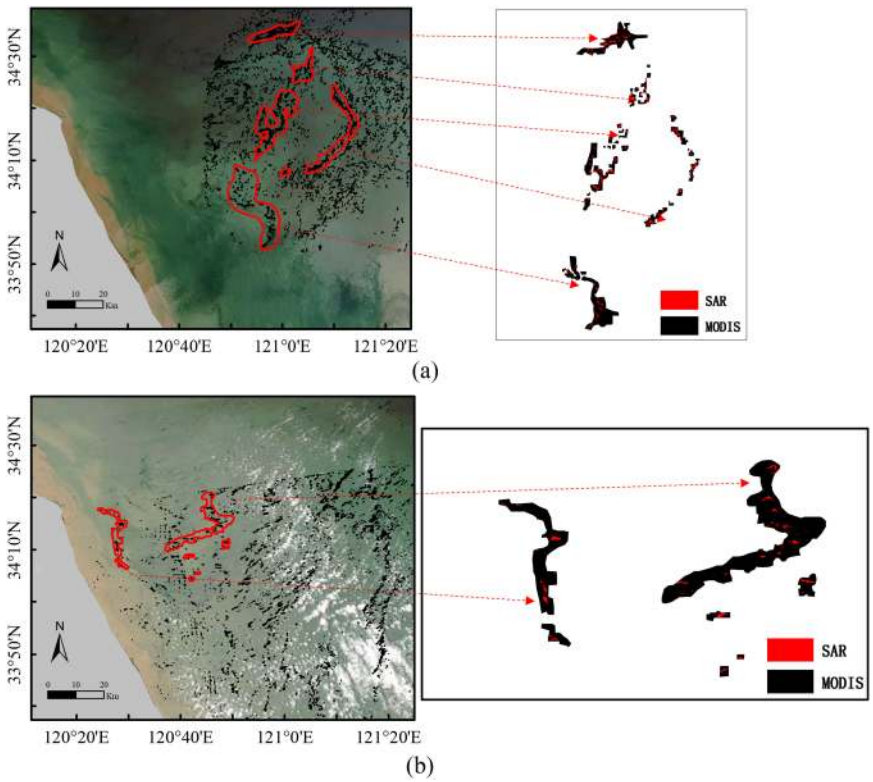


Fig. 6. Algae FS ratio in Subei Shoal: (a) Less than 5% of exposed portion of floating algae on June 23, 2018; and (b) another exposed portion example in Subei Shoal on June 11, 2019.

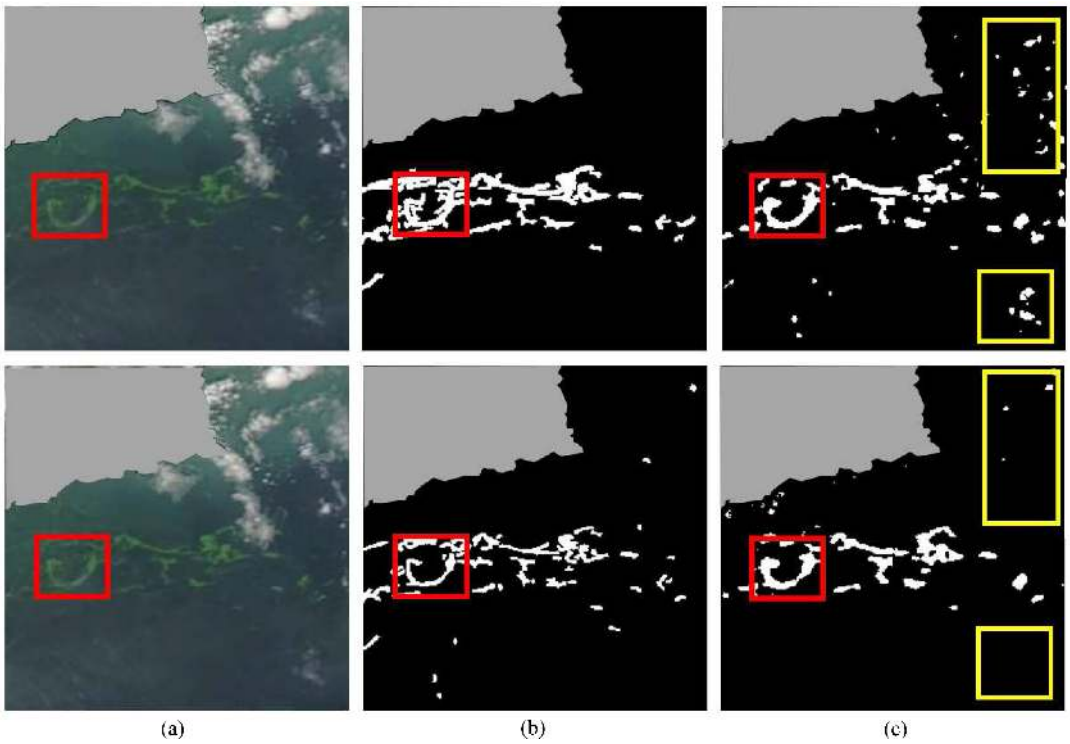


Fig. 7. Analysis of algae label uncertainty: (a) MODIS true-color image slice; (b) ground truth labels; and (c) predicted value of the AlgaeNet model. The first row is the label and predicted value before optimization and the second row is the label and predicted value after optimization.

alone. Therefore, the mean algae missing detection rate in 250-m resolution true-color MODIS imagery is 63.66%.

B. *FS Ratio in Different Life Phases in* U. Prolifera *Blooms*

U. prolifera algae rely on the thalli's hollow tubular structure to float on the sea surface, and the submerged part does not exceed 1–2 m [29]. The FS ratio reflects the changing status of floating *U. prolifera* in the Yellow Sea well. Based on the detected algae distribution, coverage, and biomass results of the 112 collected MODIS images from 2008–2021, the *U. prolifera* bloom originated from the Subei Shoal to the south of the study region, drifted northward, and experienced different phases from initiation to development, maintenance, and diminishing. For example, Fig. 1(a) and Table III show the algae distribution and coverage changes throughout the life cycle. The green polylines represent the general northern boundary of the densely distributed area in June 2013. At the various stages of the *U. prolifera* bloom, the status of floating *U. prolifera* underwent morphological changes [14], [40]. At the initiation phase in the Subei Shoal, the *U.prolifera* algae had a large proportion submerged in seawater and rare algae biomass, shown on June 02, 2013, in Fig. 1(a). Based on the two matching image pairs in Fig. 6, the FS ratio of the algae body was less than 5% (Figs. 1 and 6). During the later development phase in the Yellow Sea, the biomass of *U. prolifera* rapidly increased when they started blooming, shown on June 13 and 20, 2013, in Fig. 1(a). Moreover, a large proportion of *U. prolifera* became floating due to the optimal illumination and temperature, and the FS ratio quickly increased from less than 5% to 24.75%. Some local areas even reached more than 40%, shown as the dotted box in Fig. 1(a). During the maintenance phase of the *U. prolifera* bloom, the *U. prolifera* algae as a whole moved northward, and the biomass and FS ratio remained at a high level, basically unchanged, shown as the dotted box of ∼21.35% in Fig. 1(a). During the diminishing phase of the bloom, there were almost no algae near Subei Shoal, and the algae biomass and FS ratio in the Yellow Sea decreased rapidly to 14.33%. Therefore, in the overall life phase, the FS ratio had a parabolic process that first rose, maintained, and then fell. The rise (initiation phase) and fall (diminishing phase) were swift compared to the development and maintenance phases, shown in Fig. 1(b) and (c). Fig. 1(d) also shows the two ship surveys in the maintenance and diminishing phases. As the bloom drifts, the biomass declines rapidly and concentrates eastward. The limited biomass changes also reflect and verify the algae's life state through ship surveys. These survey results are consistent with satellite observations. Therefore, the FS ratio can be used to judge the floating algae's status at different life phases of the bloom.

V. Discussions

The difference of algae detected by MODIS and SAR can attribute to the difference of two sensors in spatial resolution, observing time, and principle of measurements. To eliminate the influence of the first two factors on the FS ratio, we made the following discussion.

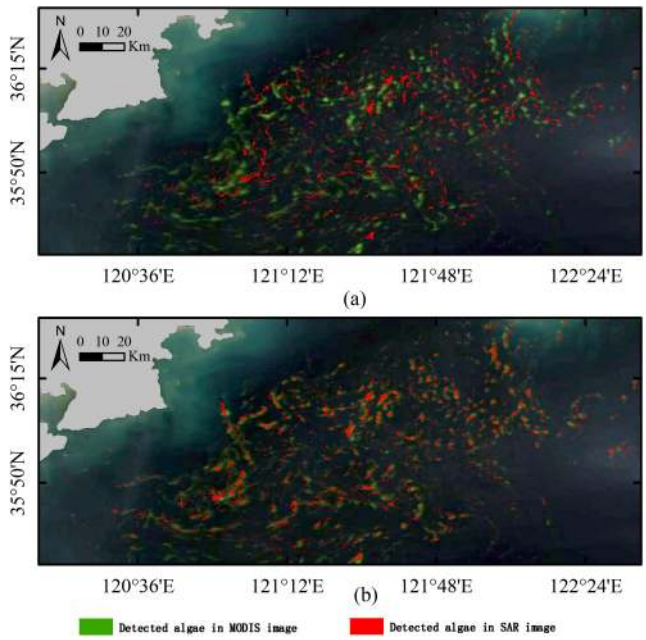


Fig. 8. Algae movement drift and registration: images before (a) and after (b) registration. The final registration residual error is less than 3 MODIS pixels.

TABLE IV
IMAGE REGISTRATION ACCURACY EVALUATION

$\overline{X}$/°	$\overline{Y}$ /°	$\overline{d}$/ °	S/ °
0.0048	0.0091	0.0113	**0.0667**

Note: $\overline{X}$ ($\overline{Y}$) represents the mean of the radial (latitudinal) difference of the feature point pairs; $\overline{d}$ represents the mean distance of the feature point pairs; and S represents the root mean square error RMSE of the distance d between the feature point pairs. After converting S from angle to distance, the maximum value of 0.0667° is 739.78 m, and the residual error is less than 3 MODIS pixels (1 pixel = 250 m).

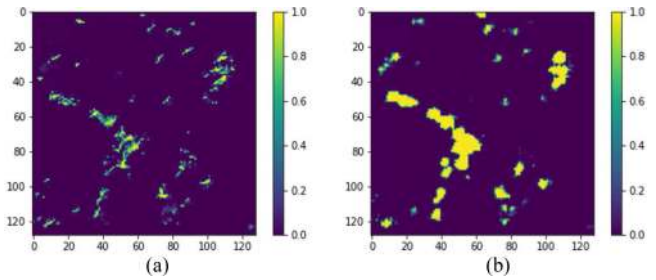


Fig. 9. Algae pixel density (a, most pixels > 0.8) and AlgaeNet output possibility (b, most pixels are close to 0.9–1.0).

A. Algae Label Uncertainty and the AlgaeNet Model's Inhibitory Effect

The AlgaeNet model needs many image labels to train the network. Although the labeling criterion has been determined according to the algae features, the labels are subject to human error. The AlgaeNet model has a particular inhibitory effect on the image labels' uncertainty (red box in Fig. 7). We can further optimize labels to improve the model according to the difference between the predicted values and the ground truth labels (yellow box in Fig. 7). DL models and label optimization are two complementary tools. High-quality labels to train the models can improve model accuracy, and DL models can also be used for label optimization to reduce artificial uncertainty.

B. Overpass Time Difference Effect

There is usually a time difference of 6–18 h between the MODIS and SAR images' acquisition times. As a result, the algae patches may have some drift and shape deformation shown in Figs. 2 and 8. Moreover, the rapid development of the algae itself should also be considered. The maximum overpass time interval is 18 h. During this long period, the algae could grow or demise a lot. Therefore, this article adopts the standard rubber sheeting method to perform image registration of algae patches in MODIS and SAR images with a registration error of fewer than three MODIS pixels (<1 km, Fig. 8 and Table IV) based on the quantitative control points and evaluation points. This small residual error will not cause a substantial impact on the accurate estimation of the algae's missing inspection rate and the FS ratio.

C. Algae Mixed Pixel and Coarse Resolution Effect

A mixed pixel issue exists in all remote sensing images. The coarser the image resolution, the greater the influence of the mixed pixels [41], [42]. For MODIS images, the influence of mixed pixels on the accuracy of algae extraction can be eliminated through the output possibility of AlgaeNet. We found that the containing-algae proportion in the MODIS pixel, i.e., algae pixel density, is almost consistent with the output possibility by the AlgaeNet model.

We use ENVI software's image mixed-pixel decomposition function to the optical image, including data dimensionality reduction, endmember selection, and spectral separation. Finally, we obtain the containing-algae proportion in each pixel. Fig. 9 also shows that the containing-algae pixel density is almost consistent with the output possibility of the AlgaeNet model. Therefore, the output possibility of the AlgaeNet model can be directly regarded as the containing-algae proportion of the algae pixel to eliminate the mixed effect. After extracting the algae-containing pixels, the corresponding pixel density can also be quantified directly using the simple unmixing method. Finally, the fractional areal coverages were estimated from all algae-containing pixels.

The above-described effect, "the broader margin of algae patches observed by MODIS compared to SAR," may be affected by the coarse resolution of MODIS (250 m) [43], [44], rather than the effect of optics (penetration) versus microwave. To verify the dependence of the FS ratio on the satellite image resolution, we added two new experiments.

Experiment 1: First, to ensure the accuracy of the FS ratio, we selected the largest possible algae patches. Then, we applied the AlgaeNet to Sentinel-2 optical images (4/3/2/8 bands and 10-m resolution), similar to Sentinel-1 and Gaofen-3 SAR resolutions. Fig. 10(a) shows that the edge of the algae patches

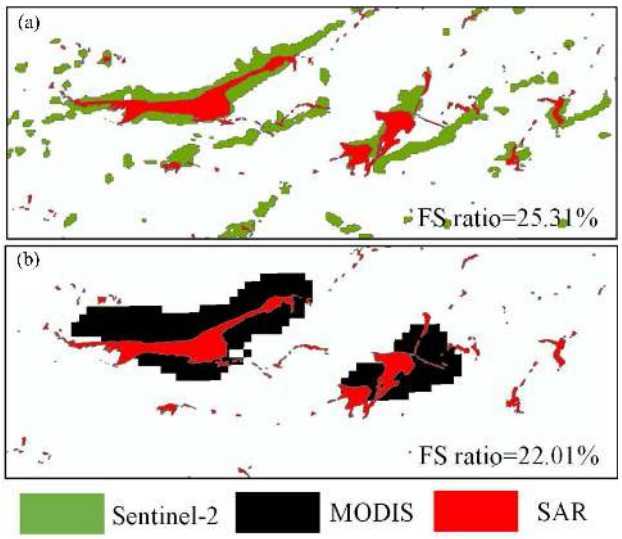


Fig. 10. Sentinel-2 (green), MODIS (black), and SAR (red) algae patches detection on June 23, 2019. It was found that the hypothesis of the "FS ratio" is valid. The figure is a part of Fig. 5.

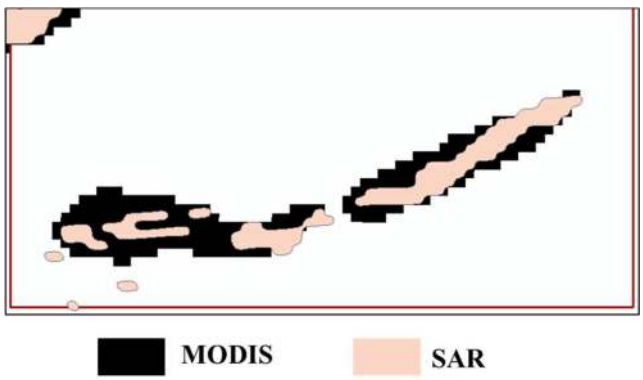


Fig. 11. MODIS (black) and resampled 250-m resolution SAR (yellow) algae patches detection. The figure is part of Fig. 5.

detected by the sentinel-2 image is larger than that by the SAR image, which preliminary proves the reliability of the "FS ratio" hypothesis we put forward. Fig. 10(a) and (b) also shows a particular difference in the algae detection results of the two optical satellite sensors, MODIS (250-m resolution) and Sentinel-2 (10-m resolution). The FS ratio estimated by MODIS has a slight difference compared with Sentinel-2 (22.01%. vs. 25.31%), which can be negligible because of such a slight difference.

Experiment 2: We resampled the SAR image from 10-m resolution to 250-m resolution, and then redetected the algae pixels on the 250-m resolution SAR image, compared it with the detection results on 250-m resolution MODIS image, and also found the broader margin of algae patches observed by MODIS compared to SAR (Fig. 11). Therefore, these two experiments proved the reliability of our model.

VI. Conclusion

U. prolifera bloom to form green tides is a disastrous ecological event in the coastal sea. Satellite remote sensing is the primary *U. prolifera* detection approach due to the frequent data acquisition and broad coverage area. In this article, a DL model, AlgaeNet, is established for detecting *U. prolifera* algae in MODIS and SAR images. We modified the model with the unique physical multichannel combination input and a new loss function design. This tailored modification improved the detection accuracy to 97.03%/99.83% and the Mean IoU to 48.57%/88.43% for MODIS/SAR images based on the labeled 1055/4071 samples pairs, among which 70%/30% were used for training/validation. The detection result of the AlgaeNet model is purely made with the optimized model weights learned from the training processes model, reducing the potential biases due to the selection of extraction thresholds during the traditional threshold-based segmentation. The other DL methods and biological indices also verified the high reliability of the AlgaeNet model. When we applied the physical input and the newly constructed loss function to the other DL models, we also achieved high accuracy, indicating the excellent portability of our unique improvement strategy in various convolutional networks.

We used the AlgaeNet model to process processed satellite images containing *U. prolifera* in the Yellow Sea and acquired 12 pairs of spatiotemporally matching MODIS and SAR images/slicks. However, due to different resolutions, observation mechanisms, and asynchronous observation (overpass time difference), the algae detection results obtained from optical and radar satellites are not entirely consistent. Compared with the traditional biological indices, the AlgaeNet model provides a more convenient fusion method to obtain two new scientific discoveries: the missing detection rate in coarse images and the FS ratio of floating algae patches. For the missing detection rate, adding high-resolution SAR image information leads to a 63.66% increase in algae detection compared to that based on MODIS imagery alone. Such a high missing inspection shows the importance of revising historical results in coarse images. On the other hand, the FS ratio of algae patches (∼5%–48.54% in different bloom phases) can be used to reflect the life status of floating *U. prolifera* algae due to the two sensors' different algae detection mechanisms.

In future article, we can further improve algae detection as follows:

1) In the 2017 ship survey, we did not conduct timely *in-situ* measurement of FS ratio due to insufficient scientific target setting. Therefore, we plan to perform the necessary ship survey and compare it with the FS ratio obtained by the AlgaeNet model to verify the constructed model further.
2) Since 2007, Sargassum golden tide and green tide have also frequently occurred together in the Yellow Sea. Therefore, the AlgaeNet model can be applied to detecting Sargassum golden tide. Furthermore, we will try to use the FS ratio to distinguish and separate the two kinds of macroalgae.

3) We can directly apply the constructed model to other marine disasters such as oil spills and further expand the applications of the AlgaeNet model.

ACKNOWLEDGMENT

The MODIS true-color.[2] Sentinel-1 SAR.[3] The Chinese GF-3 SAR images.[4] The Sentinel-2 true-color.[5]

REFERENCES

[1] D. Liu, J. K. Keesing, Q. Xing, and P. Shi, "World's largest macroalgal bloom caused by expansion of seaweed aquaculture in China," *Mar. Pollut. Bull.*, vol. 58, no. 6, pp. 888–895, Jun. 2009, doi: 10.1016/j.marpolbul.2009.01.013.

[2] L. Qi, C. Hu, Q. Xing, and S. Shang, "Long-term trend of Ulva prolifera blooms in the western Yellow Sea," *Harmful Algae*, vol. 58, pp. 35–44, 2016, doi: 10.1016/j.hal.2016.07.004.

[3] L. Hu, K. Zeng, C. Hu, and M. He, "On the remote estimation of Ulva prolifera areal coverage and biomass," *Remote Sens. Environ.*, vol. 223, pp. 194–207, 2019, doi: 10.1016/j.rse.2019.01.014.

[4] X. Lü and F. Qiao, "Distribution of sunken macroalgae against the background of tidal circulation in the coastal waters of Qingdao, China, in summer 2008," *Geophys. Res. Lett.*, vol. 35, no. 23, pp. 92–101, 2008, doi: 10.1029/2008GL036084.

[5] C. Hu *et al.*, "On the recurrent Ulva prolifera blooms in the Yellow Sea and East China Sea," *J. Geophys. Res.-Oceans*, vol. 115, no. C5, 2010, Art. no. C05017, doi: 10.1029/2009JC005561.

[6] V. Smetacek and A. Zingone, "Green and golden seaweed tides on the rise," *Nature*, vol. 504, no. 7478, pp. 84–88, 2013, doi: 10.1038/nature12860.

[7] D. Liu, J. K. Keesing, P. He, Z. Wang, Y. Shi, and Y. Wang, "The world's largest macroalgal bloom in the Yellow Sea, China: Formation and implications," *Estuarine Coastal Shelf Sci.*, vol. 129, pp. 2–10, 2013, doi: 10.1016/j.ecss.2013.05.021.

[8] F. Liu *et al.*, "Understanding the recurrent large-scale green tide in the Yellow Sea: Temporal and spatial correlations between multiple geographical, aquacultural and biological factors," *Mar. Environ. Res.*, vol. 83, pp. 38–47, Feb. 2013, doi: 10.1016/j.marenvres.2012.10.007.

[9] X. Xiao *et al.*, "Nutrient removal from Chinese coastal waters by large-scale seaweed aquaculture," *Sci. Rep.*, vol. 7, 2017, Art. no. 46613, doi: 10.1038/srep46613.

[10] J. Zhang, P. Zhao, Y. Huo, K. Yu, and P. He, "The fast expansion of pyropia aquaculture in 'Sansha' regions should be mainly responsible for the Ulva blooms in Yellow Sea," *Estuarine Coastal Shelf Sci.*, vol. 189, pp. 58–65, 2017, doi: 10.1016/j.ecss.2017.03.011.

[11] Y. Zhang *et al.*, "Ulva prolifera green-tide outbreaks and their environmental impact in the Yellow Sea, China," *Nat. Sci. Rev.*, vol. 6, no. 4, pp. 825–838, 2019, doi: 10.1093/nsr/nwz026.

[12] C. Hu, "A novel ocean color index to detect floating algae in the global oceans," *Remote Sens. Environ.*, vol. 113, no. 10, pp. 2118–2129, 2009, doi: 10.1016/j.rse.2009.05.012.

[13] J. H. Lee, I. C. Pang, I. J. Moon, and J. H. Ryu, "On physical factors that controlled the massive green tide occurrence along the southern coast of the Shandong peninsula in 2008: A numerical study using a particle-tracking experiment," *J. Geophys. Res.-Oceans*, vol. 116, 2011, Art. no. C12036, doi: 10.1029/2011jc007512.

[14] Y. Cao, Y. Wu, Z. Fang, X. Cui, J. Liang, and X. Song, "Spatiotemporal patterns and morphological characteristics of Ulva prolifera distribution in the Yellow Sea, China in 2016–2018," *Remote Sens.*, vol. 11, no. 4, 2019, Art. no. 445, doi: 10.3390/rs11040445.

[15] Q. Xing, D. An, X. Zheng, Z. Wei, and J. Chen, "Monitoring seaweed aquaculture in the Yellow Sea with multiple sensors for managing the disaster of macroalgal blooms," *Remote Sens. Environ.*, vol. 231, 2019, Art. no. 111279, doi: 10.1016/j.rse.2019.111279.

[16] C. Hu, L. Feng, R. F. Hardy, and E. J. Hochberg, "Spectral and spatial requirements of remote measurements of pelagic sargassum macroalgae," *Remote Sens. Environ.*, vol. 167, pp. 229–246, 2015, doi: 10.1016/j.rse.2015.05.022.

[2][Online]. Available: https://worldview.earthdata.nasa.gov/

[3][Online]. Available: https://search.asf.alaska.edu/

[4][Online]. Available: https://osdds.nsoas.org.cn

[5][Online]. Available: https://apps.sentinel-hub.com/eo-browser/

[17] X. Li, C. Li, Z. Yang, and W. Pichel, "SAR imaging of ocean surface oil seep trajectories induced by near inertial oscillation," *Remote Sens. Environ.*, vol. 130, pp. 182–187, 2013, doi: 10.1016/j.rse.2012.11.019.

[18] A. Lupidi, D. Staglianò, M. Martorella, and F. Berizzi, "Fast detection of oil spills and ships using SAR images," *Remote Sens.*, vol. 9, no. 3, 2017, Art. no. 230, doi: 10.3390/rs9030230.

[19] X. Geng, P. Li, J. Yang, L. Shi, X. Li, and J. Zhao, "Ulva prolifera detection with dual-polarization GF-3 SAR data," *IOP Conf. Ser., Earth Environ. Sci.*, vol. 502, no. 1, 2020, Art. no. 12026.

[20] D. Blondeau-Patissier, J. F. Gower, A. G. Dekker, S. R. Phinn, and V. E. Brando, "A review of ocean color remote sensing methods and statistical techniques for the detection, mapping and analysis of phytoplankton blooms in coastal and open oceans," *Prog. Oceanogr.*, vol. 123, pp. 123–144, 2014, doi: 10.1016/j.pocean.2013.12.008.

[21] X. Li *et al.*, "Deep learning-based information mining from ocean remote sensing imagery," *Nat. Sci. Rev.*, vol. 7, no. 10, pp. 1584–1605, 2020, doi: 10.1093/nsr/nwaa047.

[22] F. M. Bianchi, M. M. Espeseth, and N. Borch, "Large-scale detection and categorization of oil spills from SAR images with deep learning," *Remote Sens.*, vol. 12, no. 14, 2020, Art. no. 2260, doi: 10.3390/rs12142260.

[23] X. Zhang and X. Li, "Combination of satellite observations and machine learning method for internal wave forecast in the Sulu and Celebes seas," *IEEE Trans. Geosci. Remote Sens.*, vol. 59, no. 4, pp. 2822–2832, Apr. 2021, doi: 10.1109/TGRS.2020.3008067.

[24] Y. Ren, X. Li, and H. Xu, "A deep learning model to extract ship size from sentinel-1 SAR images," *IEEE Trans. Geosci. Remote Sens.*, vol. 60, 2022, Art. no. 5203414, doi: 10.1109/TGRS.2021.3063216.

[25] Y. Ren, X. Li, X. Yang, and H. Xu, "Development of a dual-attention U-Net model for sea ice and open water classification on SAR images," *IEEE Geosci. Remote Sens. Lett.*, vol. 19, Feb. 2021, Art no. 4010205, doi: 10.1109/LGRS.2021.3058049.

[26] Y. Ren, T. Cheng, and Y. Zhang, "Deep spatio-temporal residual neural network for road-network-based data modeling," *Int. J. Geogr. Inf. Sci.*, vol. 33, no. 9, pp. 1894–1912, 2019, doi: 10.1080/13658816.2019.1599895.

[27] X. Zhang, X. Li, and Q. Zheng, "A machine-learning model for forecasting internal wave propagation in the Andaman sea," *IEEE J. Sel. Topics Appl. Earth Observ. Remote Sens.*, vol. 14, pp. 3095–3106, Mar. 2021, doi: 10.1109/jstars.2021.3063529.

[28] Z. P. Lee, K. P. Du, and R. Arnone, "A model for the diffuse attenuation coefficient of downwelling irradiance," *J. Geophys. Res.-Oceans*, vol. 110, 2005, Art. no. C02016, doi: 10.1029/2004JC002275.

[29] L. Ding and R. Luan, "The taxonomy, habit, and distribution of a green alga enteromorpha prolifera (ulvales, chlorophyta)," *Oceanologia et Limnologia Sinica*, vol. 40, no. 8, pp. 68–71, 2009.

[30] J. Zhang *et al.*, "Variations of morphology and photosynthetic performances of Ulva prolifera during the whole green tide blooming process in the Yellow Sea," *Mar. Environ. Res.*, vol. 92, pp. 35–42, Dec. 2013, doi: 10.1016/j.marenvres.2013.08.009.

[31] Y. Ma, J. Zhao, W. Xie, and P. Jiang, "Branching phenotype and plasticity in floating ecotype of Ulva prolifera (Ulvophyceae, Chlorophyta)," *Mar. Sci.*, vol. 44, no. 8, pp. 98–105, Sep. 2020.

[32] B. C. Russell, A. Torralba, K. P. Murphy, and W. T. Freeman, "LabelMe: A database and web-based tool for image annotation," *Int. J. Comput. Vis.*, vol. 77, no. 1–3, pp. 157–173, 2008, doi: 10.1007/s11263-007-0090-8.

[33] O. Ronneberger, P. Fischer, and T. Brox, "U-Net: Convolutional networks for biomedical image segmentation," in *Proc. Int. Conf. Med. Image Comput. Comput.-Assisted Interv.*, 2015, pp. 234–241, doi: 10.1007/978-3-319-24574-4_28.

[34] Y. LeCun, Y. Bengio, and G. Hinton, "Deep learning," *Nature*, vol. 521, pp. 436–444, 2015, doi: 10.1038/nature14539.

[35] W. Liu, Z. Wang, X. Liu, N. Zeng, Y. Liu, and F. E. Alsaadi, "A survey of deep neural network architectures and their applications," *Neurocomputing*, vol. 234, pp. 11–26, 2017, doi: 10.1016/j.neucom.2016.12.038.

[36] B. Liu, X. Li, and G. Zheng, "Coastal inundation mapping from bitemporal and dual-polarization SAR imagery based on deep convolutional neural networks," *J. Geophys. Res.-Oceans*, vol. 124, no. 12, pp. 9101–9113, 2019, doi: 10.1029/2019JC015577.

[37] Q. Xu, H. Zhang, L. Ju, and M. Chen, "Interannual variability of ULVA prolifera blooms in the Yellow Sea," *Int. J. Remote Sens.*, vol. 35, nos. 11–12, pp. 4099–4113, 2014, doi: 10.1080/01431161.2014.916052.

[38] T. Jia, X. Zhang, and R. Dong, "Long-term spatial and temporal monitoring of cyanobacteria blooms using MODIS on Google Earth Engine: A case study in Taihu lake," *Remote Sens.*, vol. 11, no. 19, 2019, Art. no. 2269, doi: 10.3390/rs11192269.

[39] J. Hu, L. Li, Y. Lin, F. Wu, and J. Zhao, "A comparison and strategy of semantic segmentation on remote sensing images," *Adv. Natural Comput., Fuzzy Syst. Knowl. Discovery, ICNC-FSKD. Adv. Intell. Syst. Comput.*, Y. Liu, L. Wang, L. Zhao, Z. Yu, Eds., Springer, Cham, vol. 1074, pp. 21–29. 2019, doi: 10.1007/978-3-030-32456-8_3.
[40] J. Xiao *et al.*, "Decadal characteristics of the floating ULVA and sargassum in the Subei Shoal, Yellow Sea," *Acta Oceanologica Sinica*, vol. 39, no. 10, pp. 1–10, 2020, doi: 10.1007/s13131-020-1655-4.
[41] M. Wang and C. Hu, "Mapping and quantifying sargassum distribution and coverage in the Central West Atlantic using MODIS observations," *Remote Sens. Environ.*, vol. 183, pp. 350–367, 2016, doi: 10.1016/j.rse.2016.04.019.
[42] J. B. Adams, M. O. Smith, and P. E. Johnson, "Spectral mixture modeling: A new analysis of rock and soil types at the Viking Lander 1 site," *J. Geophys. Res., Solid Earth*, vol. 91, no. B8, pp. 8098–8112, 1986, doi: 10.1029/JB091iB08p08098.
[43] Q. Xu, H. Zhang, and Y. Cheng, "Multi-sensor monitoring of ULVA prolifera blooms in the Yellow Sea using different methods," *Front. Earth Sci.*, vol. 10, pp. 378–388, 2016, doi: 10.1007/s11707-015-0528-1.
[44] T. Cui *et al.*, "Assessing and refining the satellite-derived massive green macro-algal coverage in the Yellow Sea with high resolution images," *ISPRS J. Photogramm. Remote Sens.*, vol. 144, pp. 315–324, 2018, doi: 10.1016/j.isprsjprs.2018.08.001.



Le Gao (Member, IEEE) received the B.S. degree in geodesy and surveying engineering from the Shandong University of Science and Technology, Qingdao, China, in 2008, the joint M.S. degree in cartography and geography information system from the Shandong University of Science and Technology, Qingdao, China, and Chinese Academy of Surveying and Mapping, Beijing, China, in 2011, and the joint Ph.D. degree in cartography and geography information system from the Institute of Remote Sensing and Digital Earth, Chinese Academy of Sciences, Beijing, China, and Space Research Institute, Austrian Academy of Sciences, Graz, Austria, in 2014.

He is an Associate Professor with the Key Laboratory of Ocean Circulation and Waves, Institute of Oceanology, Chinese Academy of Sciences, Qingdao, China. His research interests include artificial intelligence oceanography, big data, target detection and semantic segmentation from ocean remote sensing data, and ocean prediction based on deep learning.



Xiaofeng Li (Fellow, IEEE) received the B.S. degree in optical engineering from Zhejiang University, Hangzhou, China, in 1985, the M.S. degree in physical oceanography from the First Institute of Oceanography, Qingdao, China, in 1992, and the Ph.D. degree in physical oceanography from North Carolina State University, Raleigh, NC, USA, in 1997.

He was with the National Environmental Satellite, Data, and Information Service, National Ocean and Atmospheric Administration, USA, from 1997 to 2019. He is currently with the Institute of Oceanology, the Chinese Academy of Sciences. His research interests include synthetic aperture radar oceanography and marine meteorology, artificial intelligence oceanography, big data, and satellite image processing.

Dr. Li is an Associate Editor of the IEEE TRANSACTIONS ON GEOSCIENCE AND REMOTE SENSING and *International Journal of Remote Sensing*. In addition, he is an Editorial Board Member of the *International Journal of Digital Earth*, *Big Earth Data,* and *Journal of Oceanology and Limnology*. He is also the Executive Editor-in-Chief of *Journal of Remote Sensing* (a Science Partner Journal).



Fanzhou Kong received the B.S. and M.S. degrees in marine biology from the Ocean University of China, Qingdao, China, in 2001 and 2007, and the Ph.D. degree in environmental science from the Institute of Oceanology, Chinese Academy of Sciences, Qingdao, China, in 2011.

He is currently an Associate Professor with the Department of Key Laboratory of Marine Ecology and Environmental Sciences, Institute of Oceanology, Chinese Academy of Sciences. His research interests include harmful algal bloom and phytoplankton pigments.



Rencheng Yu received the B.S. degree in environmental science from Nankai University, Tianjin, China, in 1993, and the Ph.D. degree in marine biology from the Institute of Oceanology, Chinese Academy of Sciences, Qingdao, China, in 1998.

He is currently a Professor and the Director with the Key Laboratory of Marine Ecology and Environmental Sciences, Institute of Oceanology. His research interests include ecology and oceanography of harmful algal blooms and phycotoxin analysis.



Yuan Guo (Student Member, IEEE) received the B.S. degree in remote sensing science and technology from the Anhui University of Science and Technology, Anhui, China, in 2020. She is currently working toward the M.S. degree in physical oceanography at the Institute of Oceanology, Chinese Academy of Sciences, Qingdao, China.

Her research interest includes deep-learning semantic segmentation from ocean remote sensing data.



Yibin Ren (Member, IEEE) received the B.S. degree in geographical information science from the Shandong University of Science and Technology, Qingdao, China, in 2012, the M.S. degree in cartography and geography information system from the Nanjing University, Nanjing, China, in 2015, and the joint Ph.D. degree in cartography and geography information system from the Ocean University of China and the University College London, London, U.K., in 2019.

He is currently an Assistant Researcher with the Key Laboratory of Ocean Circulation and Waves, Institute of Oceanology, Chinese Academy of Sciences, Qingdao, China. His research interests include target detection and semantic segmentation from ocean remote sensing data and ocean prediction based on deep learning.